RESEARCH ARTICLE

WILEY

Sodium-rich NASICON-structured cathodes for boosting the energy density and lifespan of sodium-free-anode sodium metal batteries

Junxiong Wu[1,2] | **Cong Lin[1]** | **Qinghua Liang[3]** | **Guodong Zhou[4]** | **Jiapeng Liu[4]** | **Gemeng Liang[5]** | **Man Wang[1]** | **Baohua Li[6]** | **Liang Hu[1]** | **Francesco Ciucci[4]** | **Qiang Liu[1]** | **Guohua Chen[1]** | **Xiaoliang Yu[1]**

[1]Department of Mechanical Engineering, Research Institute for Smart Energy, The Hong Kong Polytechnic University, Hong Kong, China

[2]College of Environmental Science and Engineering, Fujian Normal University, Fuzhou, Fujian, China

[3]Department of Chemical Engineering, The University of Melbourne, Parkville, Victoria, Australia

[4]Department of Mechanical and Aerospace Engineering, The Hong Kong University of Science and Technology, Hong Kong, China

[5]Institute for Superconducting & Electronic Materials, University of Wollongong, Wollongong, New South Wales, Australia

[6]Shenzhen Key Laboratory on Power Battery Safety and Shenzhen Geim Graphene Center, Tsinghua Shenzhen International Graduate School (SIGS), Shenzhen, China

Correspondence
Baohua Li, Shenzhen Key Laboratory on Power Battery Safety and Shenzhen Geim Graphene Center, Tsinghua Shenzhen International Graduate School (SIGS), Shenzhen, China.
Email: libh@mail.sz.tsinghua.edu.cn

Guohua Chen and Xiaoliang Yu, Department of Mechanical Engineering, Research Institute for Smart Energy, The Hong Kong Polytechnic University, Hong Kong, China.
Email: guohua.chen@polyu.edu.hk and xiaoliang.yu@polyu.edu.hk

Abstract

Rechargeable sodium metal batteries (SMBs) have emerged as promising alternatives to commercial Li-ion batteries because of the natural abundance and low cost of sodium resources. However, the overuse of metallic sodium in conventional SMBs limits their energy densities and leads to severe safety concerns. Herein, we propose a sodium-free-anode SMB (SFA-SMB) configuration consisting of a sodium-rich Na superionic conductor-structured cathode and a bare Al/C current collector to address the above challenges. Sodiated $Na_3V_2(PO_4)_3$ in the form of $Na_5V_2(PO_4)_3$ was investigated as a cathode to provide a stable and controllable sodium source in the SFA-SMB. It provides not only remarkable Coulombic efficiencies of Na plating/stripping cycles but also a highly reversible three-electron redox reaction within 1.0–3.8 V versus Na/Na$^+$ confirmed by structural/electrochemical measurements. Consequently, an ultrahigh energy density of 400 Wh kg^{-1} was achieved for the SFA-SMB with fast Na storage kinetics and impressive capacity retention of 93% after 130 cycles. A narrowed voltage window (3.0–3.8 V vs. Na/Na$^+$) further increased the lifespan to over 300 cycles with a high retained specific energy of 320 Wh kg^{-1}. Therefore, the proposed SFA-SMB configuration opens a new

avenue for fabricating next-generation batteries with high energy densities and long lifetimes.

KEYWORDS

high energy density, long lifespan, presodiation, sodium-free-anode, sodium metal batteries

1 | INTRODUCTION

Despite their commercial success in portable electronic devices and electric vehicles, lithium-ion batteries (LIBs) have nearly approached the maximum energy densities.[1–6] In addition, the increased concerns for the availability and cost of Li on the earth have to be addressed considering the increasing demand for LIBs for electric vehicles and energy storage.[7] Rechargeable sodium batteries are widely recognized as attractive alternatives, regarding the cost-effectiveness, elemental abundance, and uniform geographic distribution of Na-containing precursors.[8–14] Among them, sodium metal batteries (SMBs) are highly promising for next-generation high-energy devices because metallic Na exhibits a remarkable theoretical specific capacity of 1165 mAh g^{-1} and low redox potential of -2.71 V versus standard hydrogen electrode.[15,16] However, the ultrahigh reactivity of Na metal with liquid electrolytes usually results in an unstable solid electrolyte interphase (SEI) formation and serious Na dendrite growth during Na plating/stripping cycles. To mitigate the issue of poor cycle life and safety concerns in SMBs, substantial studies have been carried out, including optimization of the electrolyte formula,[17,18] construction of artificial SEI layers,[19] modulation of current collectors and sodium hosts,[15,20–23] creation of functional interlayers,[16] and utilization of solid-state electrolytes.[24,25] Thick Na foils were used in these studies. Although the almost infinite Na supply artificially prolongs the battery lifespan, the energy density of SMBs will be compromised. Thus, the utilization of a thin Na foil would be favorable, yet the processing is quite complicated and cost-expensive.[26] Therefore, alternative strategies are highly desired to address the above issues of SMBs to simultaneously achieve a high energy density and good processability.

To maximize the energy density and eliminate the initial use of reactive metallic Na anode during cell fabrication, a sodium-free-anode configuration has recently been proposed.[27–33] A typical sodium-free-anode SMB (SFA-SMB, also known as anode-free SMB) comprises a Na-containing cathode, a bare anode current collector (e.g., Al or Cu foil), a separator, and an appropriate amount of organic liquid electrolyte. To achieve a long cycle life in SFA-SMB, optimization of the cathode, anode, and electrolyte is required. In a pioneering study, Pint et al. paired a presodiated pyrite cathode with a nanocarbon-coated Al foil.[27] Although a high energy density of ~400 Wh kg^{-1} was achieved, the poor redox cyclic stability of the cathode should be addressed for the SFA-SMB. They then replaced the presodiated pyrite with a $Na_3V_2(PO_4)_3$ (Na3VP) cathode to realize an improved cyclability of the cell with capacity retention of 82.5% after 100 cycles at C/3.[22] Likewise, sodium iron hexacyanoferrate ($Na_2Fe_2[CN]_6$) materials were explored as stable cathodes for SFA-SMBs.[31,32] To improve the Na plating/stripping efficiency at the anode side, abundant Na nucleation sites were provided to promote a uniform Na deposition.[28] An advanced glyme-based liquid electrolyte was also developed to induce shiny-smooth nonporous Na metal deposition.[33] Despite these advances, current SFA-SMBs still suffer from a short lifespan originating from the continuous depletion of Na and electrolytes during charge/discharge cycling.

Recently, the introduction of preloaded Li sources at the cathode side has attracted increasing interest to offset the Li loss during cycling in "Li-free" lithium metal batteries.[34,35] Considering the structural diversity of sodium cathodes, this is very promising for the fabrication of sodium-rich cathodes in SFA-SMBs to extend their lifespan and expand their practical applications. Current presodiation strategies rely mainly on the implantation of sodiation agents in sodium cathodes, such as $Na_2C_4O_4$,[36] $Na_2C_2O_4$,[37] Na_2S,[38] Na_3P,[39] and NaN_3.[40] However, the introduction of inactive species and possible generation of N_2/CO_2 gases during the pre-charge process are detrimental to the energy density, cycle life, and safety of batteries.[41] Chemical presodiation is another promising approach without importing undesirable components. However, it inevitably requires complex processing steps in an inert-gas protected environment.[42,43]

In this study, we devise a presodiation strategy to pre-store a large amount of Na in Na superionic conductor (NASICON)-structured cathodes with stable structures.[44] Specifically, the presodiated Na3VP in the form of $Na_5V_2(PO_4)_3$ (Na5VP) can be directly used as a working electrode in SFA-SMBs to concurrently improve the energy density and prolong the cycle life. As illustrated in Figure 1A, during the sodiation process, two more Na atoms can be gradually inserted into the Na3VP lattice associated with the phase transformation from Na3VP to $Na_4V_2(PO_4)_3$ (Na4VP) and finally to Na5VP. In the desodiation process, two Na atoms are reversibly
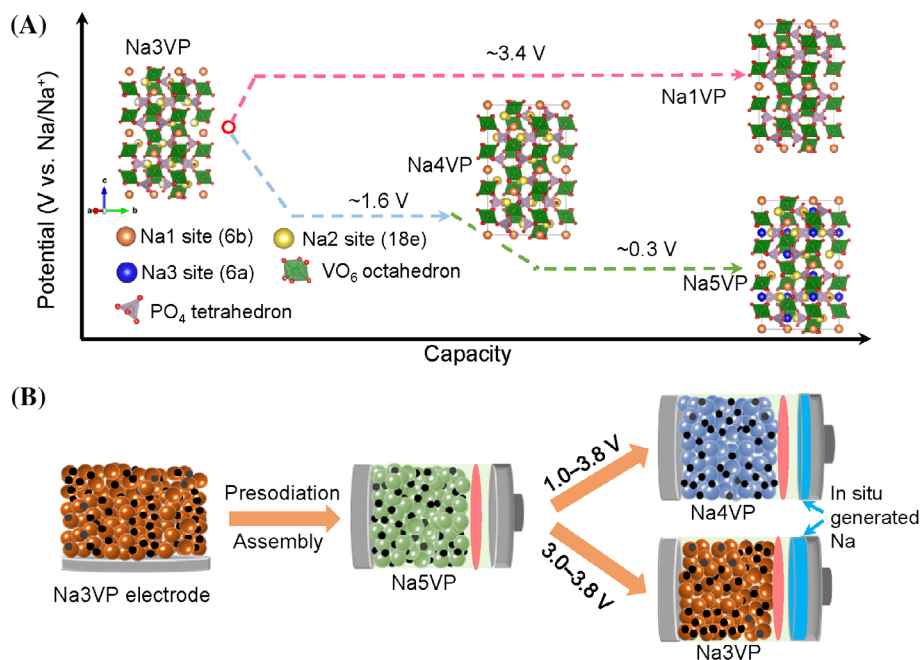
FIGURE 1 The concept of sodium-rich NASICON-structured cathodes for advanced SFA-SMBs. (A) Schematic illustrating the phase transitions of Na3VP during sodiation and desodiation. (B) Illustration of presodiation, assembly, and operation of SFA-SMB cells in two different voltage windows. During the initial charge process of the SFA-SMB cell, four Na per formula of Na5VP can be extracted and deposited onto the Al/C current collector, accompanying the formation of Na1VP. Afterward, the battery is charged and discharged within a selected voltage window, for example, 1.0–3.8 or 3.0–3.8 V versus Na/Na$^+$ to proceed with a three- or two-electron redox reaction, respectively. SFA, sodium-free-anode; SMBs, sodium metal batteries

extracted from Na3VP to form $Na_1V_2(PO_4)_3$ (Na1VP). Encouraged by the highly reversible phase transitions, we fabricated an SFA-SMB cell of Na5VP‖carbon-coated Al (Al/C), as shown in Figure 1B. The prestored Na atoms in Na5VP not only act as ideal Na replenishers to offset the loss of Na during cycling but also enable the reversible three-electron redox reaction within the voltage window of 1.0–3.8 V versus Na/Na$^+$. Thus, they offer a remarkable energy density of 400 Wh kg^{-1} (based on the total mass of active materials) and long cycle life. For operation in a narrow voltage window (3.0–3.8 V vs. Na/Na$^+$), the SFA-SMBs exhibited improved cyclic stability with a capacity retention of 95% over 300 cycles at 2C. The proposed reversible sodiation strategy in SFA-SMBs opens a new avenue for the construction of high-energy and long-life batteries.

2 | RESULTS AND DISCUSSION

2.1 | Reversible sodiation of Na3VP cathode

Na3VP is an NASICON with an open 3D structure for fast Na$^+$ transportation.[14,45] A commercially available Na3VP material was used in this work. The powder x-ray

diffraction (XRD) pattern and the corresponding Rietveld refinement confirm the high purity of the rhombohedral Na3VP with R$\bar{3}$c space group (Figure S1). The refined parameters ($a = b = 8.724\,Å$, $c = 21.805\,Å$, and $V = 1439.2\,Å^3$) agree well with previous reports.[46,47] The survey of x-ray photoelectron spectrum (XPS) reveals the presence of Na, V, O, P, and C elements (Figure S2A). The V 2p spectrum displays two peaks located at 516.7 and 524.0 eV (Figure S2B), corresponding to the V 2p$_{3/2}$ and V 2p$_{1/2}$ of V^{3+}, respectively.[48] The morphology and microstructure of the Na3VP were studied using scanning electron microscopy (SEM) and transmission electron microscopy (TEM). The Na3VP features a spherical morphology with a diameter ranging from 5 to 20 μm (Figure S3). The TEM image confirms the solid globular microstructure of the Na3VP microsphere (Figure S4A). The scanning TEM (STEM) image shows that the Na3VP microspheres are composed of smaller nanoparticles and well-connected carbon matrices. The corresponding energy-dispersive x-ray spectroscopy (EDS) mapping reveals that Na, V, P, and O elements surrounded by carbon are uniformly distributed around the Na3VP nanoparticle (Figure S5). The high-resolution TEM image of the Na3VP nanoparticles clearly shows the lattice fringes for the (104) plane with a d-spacing of 0.435 nm, in agreement with the XRD result. Moreover, the Na3VP

nanoparticles are enwrapped with a thin and conformal carbon layer of ~6–8 nm in thickness (Figure S4B), which offers a decent electronic conducting network for good rate capability.[49] Such secondary Na3VP microspheres composed of nanosized primary particles encapsulated in the carbon layer not only show good processability for fabricating homogeneous and dense electrodes but favor fast ion/electron transportation and superior structural stability.[50–52]

The sodiation behavior of Na3VP was first investigated by discharging Na3VP||Na half-cells. As shown in Figure 2A, two characteristic plateaus at ~1.6 and ~0.22 V were observed, which can be assigned to the redox couples of $V^{3+}/V^{3+/2+}$ and $V^{3+/2+}/V^{2+}$, respectively.[46,53] The plateau at ~1.6 V is associated with the insertion of the first Na atom at the remaining 18e site, corresponding to a specific capacity of 60 mAh g_{Na3VP}^{-1}. Upon further sodiation, the empty 6a site is then filled with another Na atom

associated with a specific capacity of ~100 mAh g_{Na3VP}^{-1} for sodiation. Notably, this value is higher than the theoretical capacity (~60 mAh g_{Na3VP}^{-1}) for the insertion of the second Na ion, in agreement with a previous report.[46] The additional capacity may be contributed by the carbon additives and SEI formation. The cyclic voltammetry (CV) curves were further measured to confirm the reversibility of the Na insertion/extraction for the Na3VP electrode (Figure 2B). Two pairs of cathodic/anodic peaks located at ~0.22/0.35 and ~1.6/1.78 V are in accord with plateaus observed in the galvanostatic charge/discharge profiles. The cathodic/anodic peaks at ~3.35/3.45 V can be indexed to the redox couple of V^{3+}/V^{4+}, agreeing well with previous results.[49] The almost overlapped CV curves after the initial cycle indicate the highly reversible phase transition of Na3VP upon sodiation and desodiation.

Furthermore, we performed operando XRD to study the phase transition during charging/discharging in the
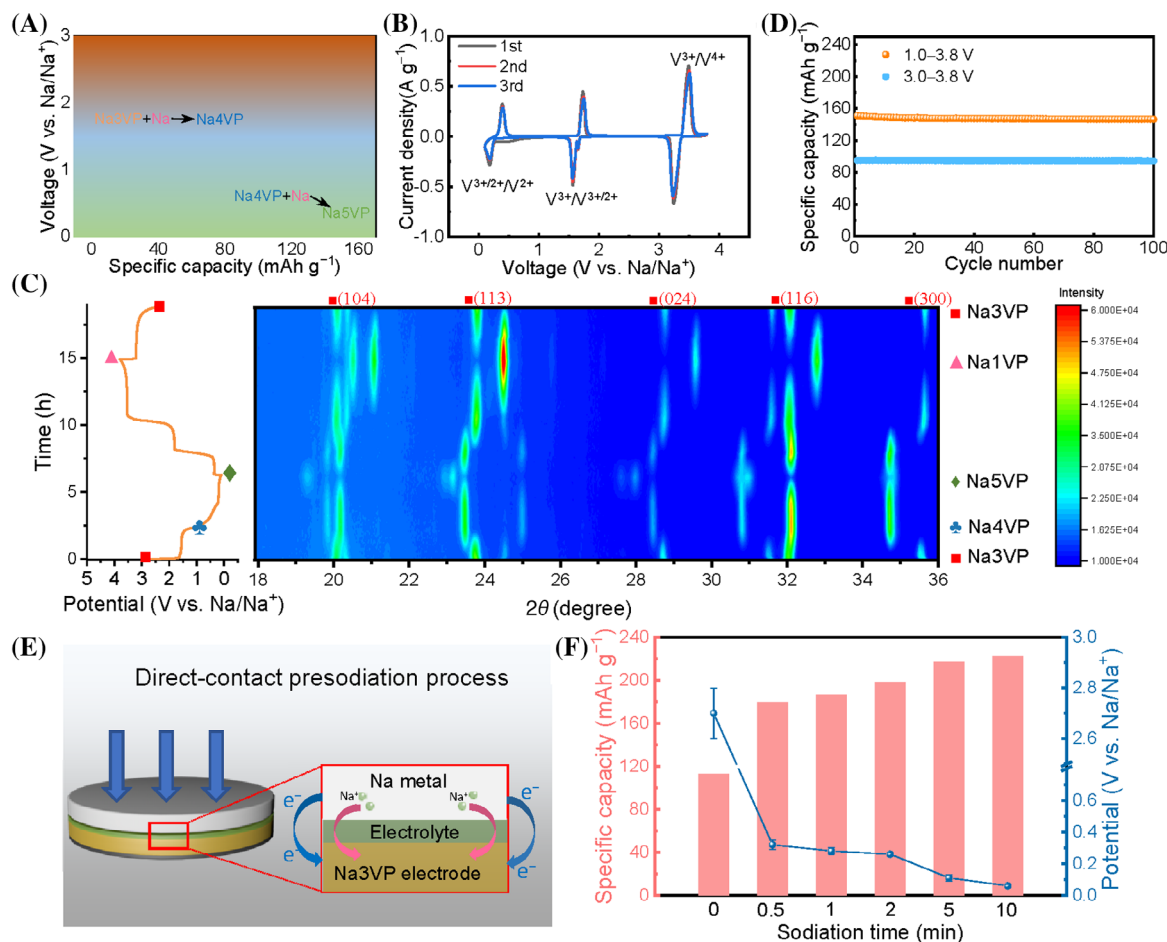

FIGURE 2 Presodiation of Na3VP cathode. (A) Voltage profile during the first discharge to 0.1 V versus Na/Na⁺. (B) CV curves of a Na3VP||Na cell within the voltage range of 0.1–3.8 V. (C) Contour plot of operando XRD patterns of a Na3VP||Na cell in a 2θ of 18–36° along with corresponding voltage profiles. (D) Cyclic performance of Na5VP||Na cells within different voltage windows (1.0–3.8 and 3.0–3.8 V). (E) Schematic showing the short-circuit presodiation process. (F) Comparison of the initial charge capacity and OCV of the presodiated Na$_{3+x}$V$_2$(PO$_4$)$_3$ ($0 \leq x \leq 2$) electrodes after different sodiation periods. CV, cyclic voltammetry; OCV, open-circuit voltage; XRD, x-ray diffraction

voltage range of 0.1–3.8 V (Figure 2C). During the first discharge to 1.0 V, the diffraction peaks corresponding to the (113), (024), (116), and (300) planes of Na3VP became weaker and gradually shifted to smaller angles. Simultaneously, the appearance of several peaks at 28.5°, 30.8°, and 34.7° can be attributed to the phase transition from Na3VP to Na4VP. Upon a further sodiation to 0.1 V, the insertion of Na ions resulted in disappearance of the (024) and (116) peaks, indicating that the Na4VP was converted to Na5VP. Moreover, the powder XRD pattern of the Na5VP electrode and corresponding Rietveld refinement revealed that the Na5VP electrode still contained about 10 wt% Na4VP and the lattice constants of Na5VP were $a = 15.508$ Å, $b = 8.894$ Å, $c = 22.708$ Å, and $\beta = 89.215°$ in the C2/c space group (Figure S6). During the charge process from 0.1 to 3.0 V, the Na5VP gradually transformed into Na3VP, as confirmed by the recurring of typical diffraction peaks for Na3VP. Further charging led to the emergence of the Na1VP phase, as indicated by new diffraction peaks at 24.8°, 29.8°, and 33° with gradually increased intensity. When the cell was charged to 3.8 V, all diffraction peaks can be well indexed to Na1VP. Upon a desodiation to 2.5 V, the characteristic peaks of Na1VP diminished, accompanying the formation of Na3VP. The operando XRD confirmed the highly reversible insertion/extraction of Na in Na3VP, accounting for the excellent structural stability.

The structural stability of the electrode materials is critical to battery performance. Therefore, we calculated the volume change of Na3VP during charge/discharge using density functional theory (DFT) calculations. The structures of Na1VP, Na3VP, Na4VP, and Na5VP were fully relaxed and the corresponding lattice parameters are summarized in Table S1. The obtained lattice parameters are slightly larger than the previously reported experimental values but within an acceptable deviation below 5%.[49] The theoretical results demonstrated that the volume shrinkage from Na3VP to Na1VP is ~9.2%, which is close to the experimental value of 8.3%.[49] Meanwhile, the insertion of one and two Na per formula Na3VP gives rise to a volume expansion of ~3.1% and 11.2%, respectively. We further analyzed the morphology changes of the as-fabricated Na3VP and Na5VP electrodes. The Na3VP microspheres were uniformly distributed around the electrode (Figure S7A,B). After the initial sodiation process to 0.1 V, the Na5VP maintained its spherical morphology without cracks. The observed thin film covering the surfaces of the Na5VP microspheres may be attributed to the SEI originating from the decomposition of the electrolyte (Figure S7C,D). Overall, the Na3VP electrode exhibited negligible morphological changes upon the sodiation process, which indicates good structural integrity of Na3VP. In addition, the Na5VP also exhibited a similar spherical morphology to that of Na3VP according to the TEM (Figure S8A). The high-resolution TEM image of Na5VP showed a d-spacing of 0.290 nm, corresponding to the lattice fringes for the (116) plane (Figure S8B).

To evaluate the reversibility of multi-electron cathodic redox reaction in SFA-SMBs, we measured the cyclic performance of Na5VP||Na cells within different voltage windows at 1C (1C = 110 mA g^{-1}). As shown in Figure 2D, the Na5VP electrode delivered a specific capacity of ~150 mAh g$_{Na5VP}^{-1}$ at 1C as the lower cutoff voltage is 1.0 V versus Na/Na$^+$. When the voltage window was limited within 3.0–3.8 V versus Na/Na$^+$, the corresponding specific capacity was determined to be ~97 mAh g$_{Na5VP}^{-1}$. The cells for working in both two voltage windows showed outstanding cyclic stability, indicating the marginal structural degradation during cycling. The cyclic performance of Na3VP||Na cell was also examined for comparison (Figure S9). The Na5VP||Na cell showed quite similar cyclic stability to the Na3VP||Na cell within the same voltage window. The excellent structural stability of the cathode during charge/discharge processes is crucial for SFA-SMBs to achieve a long cycle life.

To investigate the practical feasibility of SFA-SMBs, we developed a simple and scalable direct-contact method to prepare a Na5VP electrode. As illustrated in Figure 2E, after placing Na metal on the Na3VP electrode wetted with 20 μl of electrolyte, a potential gradient between the two electrodes engenders the flow of electrons from Na to Na3VP. Meanwhile, Na ions can smoothly intercalate into the Na3VP electrode through a rapid bulk diffusion to maintain charge neutrality. As a result, sodium-rich Na$_{3+x}$V$_2$(PO$_4$)$_3$ ($0 \leq x \leq 2$) electrodes were obtained. As the reaction time was increased from 0 to 10 min, the open-circuit voltage (OCV) of the as-fabricated Na$_{3+x}$V$_2$(PO$_4$)$_3$||Na half-cell continuously decreased, whereas the initial charge (Na extraction) capacity of the presodiated Na$_{3+x}$V$_2$(PO$_4$)$_3$ electrode increased (Figure 2F), suggesting a sustained Na insertion reaction during the direct-contact presodiation process. When the sodiation time was longer than 5 min, a fully sodiated Na5VP was obtained, as indicated by the almost constant OCV and Na extraction capacity. These results suggest that the direct-contact method is simple and controllable for the preparation of sodiated electrodes, which is promising for large-scale applications.

2.2 | Sodium plating/stripping stability

The Na Coulombic efficiency (CE) during platting/stripping for SFA-SMBs is of great significance for evaluating the cycle life. The Al and Al/C substrates were

selected as the anode current collectors because Al-based current collectors are inexpensive and light in weight. As shown in Figure 3A, the Al/C electrode exhibited relatively high and stable CEs of ≈99.8% for 300 cycles at an areal current of 0.5 mA cm^{-2} with a deposition capacity of 1.0 mAh cm^{-2}. By contrast, the bare Al foil displayed fluctuating CEs after only 25 cycles, which may be attributed to the formation of Na dendrites. It is worth noting that the Al/C current collector maintained stable overpotentials and nearly overlapping of voltage profiles over prolonged 300 cycles, while the Na plating/stripping CEs vibrated when bare Al was used as the current collector (Figure S10). As compared in Figure 3B, the Al/C current collector displayed a much lower plating nucleation overpotential (33 mV) than the Al counterpart (110 mV) at a current density of 0.5 mA cm^{-2}. The much smaller nucleation barrier suggests that the carbon layer of Al/C can offer abundant nucleation sites to guide the nucleation and propagation of metallic Na. Moreover, the morphologies of the deposited Na on Al/C and Al foils were observed by SEM. As shown in Figure 3C,D, the deposited Na on Al/C current collector was much more uniform and denser than that on the Al foil, leading to a smaller surface area for side reactions with the electrolyte. The optical and cross-section SEM images also demonstrated a more homogenous Na deposition on Al/C substrate without obvious dendrite formation, which accounts for the highly stable Na plating/stripping on Al/C current collector (Figure S11).

The Na plating/stripping CE at higher areal currents was also assessed. As shown in Figure 3E, the Al/C current collector showed CEs of 99.8%, 99.7%, and 98.9% at areal currents of 1.0, 2.0, and 4.0 mA cm^{-2}, respectively. In contrast, the Al current collector displayed highly fluctuating CEs at various areal currents. Notably, the Al/C current collector showed a much lower overpotential of 44 mV at 4.0 mA cm^{-2} than that on Al foil (64 mV), implying the excellent rate capability of the Al/C electrode (Figures 3F and S12). The above results demonstrate that the Al/C current collector enables higher and much more stable Na plating/stripping CEs, accounting for the highly reversible Na deposition and dissolution. Therefore, the Al/C substrate was selected as the current collector to assemble SFA-SMBs.

2.3 | Electrochemical performance of SFA-SMBs

Encouraged by the outstanding cyclic stability of the presodiated electrodes and impressive Na plating/ stripping CE on Al/C current collector, the Na5VP||Al/C (cathode||anode) SFA-SMBs with a supplementary Na source on the cathode side were assembled. Notably, the Na5VP electrodes used in the fabrication of SFS-SMBs were prepared using the galvanostatic discharge method, unless otherwise specified. A Na3VP||Al/C cell without Na replenisher was also fabricated and tested as a
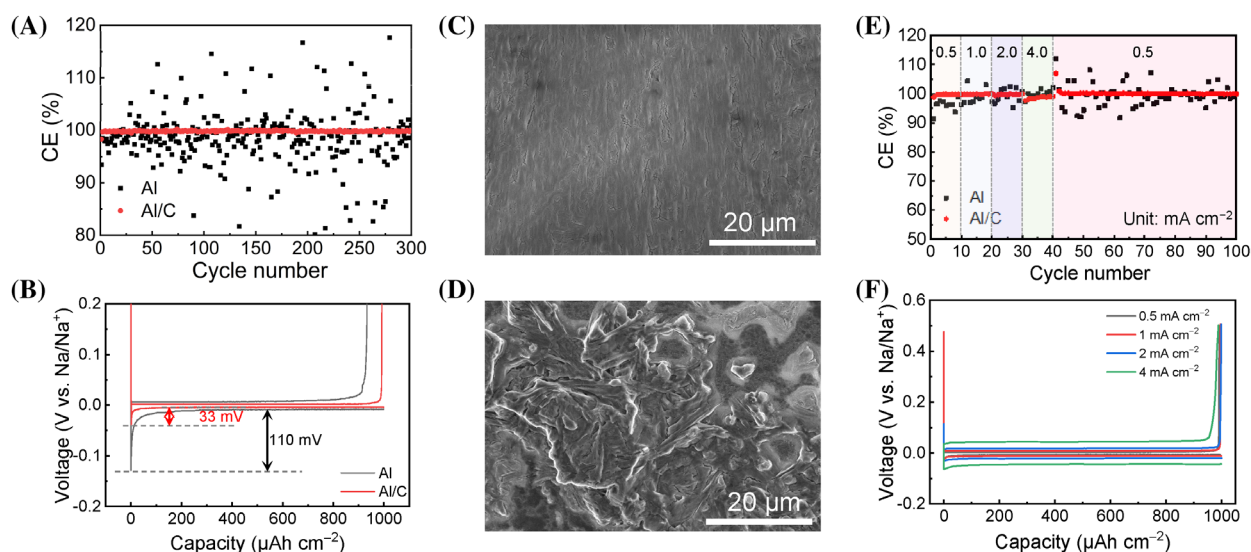

FIGURE 3 Sodium plating/stripping behaviors on Al/C and Al current collectors. (A) CEs and (B) voltage profiles of Na||Al/C and Na||Al cells at 0.5 mA cm^{-2} with a Na deposition capacity of 1.0 mAh cm^{-2}. SEM images of the deposited Na on (C) Al/C and (D) bare Al current collectors after plating Na with a capacity of 2.0 mAh cm^{-2} at 0.5 mA cm^{-2}. (E) CEs of Na||Al/C and Na||Al cells at various areal currents with a deposition capacity of 1.0 mAh cm^{-2}, and (F) corresponding voltage profiles of Na||Al/C cells. CEs, Coulombic efficiencies; SEM, scanning electron microscopy
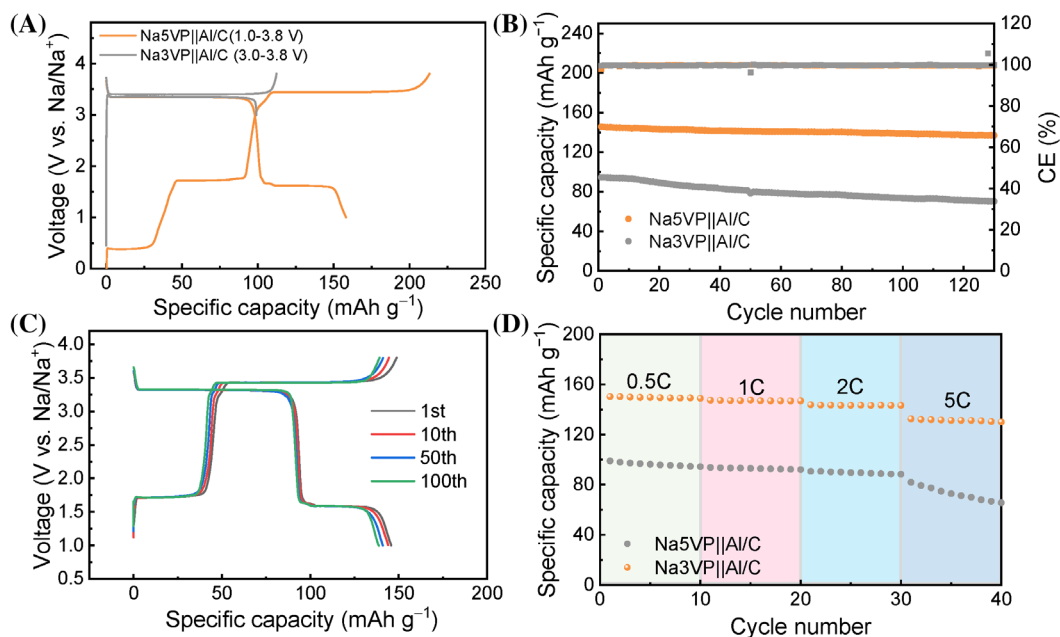
FIGURE 4 Electrochemical performance of the Na5VP||Al/C cells within the voltage window of 1.0–3.8 V. (A) Initial GCD profiles of Na5VP||Al/C and Na3VP||Al/C cells at 0.5C. (B) Cyclic performance and (C) corresponding GCD profiles at 2C. (D) Rate capability at various current densities from 0.5C to 5C. GCD, galvanostatic charge–discharge; SFA, sodium-free-anode; SMBs, sodium metal batteries

reference. As shown in Figure 4A, the galvanostatic charge–discharge (GCD) curves for the Na5VP||Al/C cell showed two additional plateaus at 0.35 and 1.7 V versus Na/Na$^+$ during the first charge process, corresponding to extraction of the presodiated Na from the Na5VP electrode. The initial charge capacity of the Na5VP electrodes was ~200 mAh g_{Na5VP}^{-1} (225 mAh g_{Na3VP}^{-1}). For comparison, the Na3VP electrode exhibited a charge capacity of 115 mAh g_{Na3VP}^{-1}, quite close to the theoretical value. The different charge capacities of the Na5VP and Na3VP electrodes indicate that a specific capacity of 110 mAh g_{Na3VP}^{-1} of sodium was prestored in the Na5VP cathodes, which can serve as an ideal Na supplement to offset the Na loss during cycling. Moreover, the initial CE of the Na3VP||Al/C cell was 90%. The deviation of the CE from 100% is largely attributed to the oxidation of the electrolyte at the cathode side as well as the sodiation of the carbon layer and the formation of the SEI.[22]

Recall that volume expansion from Na3VP to Na5VP is considerably larger than that from Na3VP to Na4VP according to the DFT calculations. In addition, the V^{3+}/ V$^{3+/2+}$ redox reaction occurring at a relatively low potential of ~0.3 V contributes to the limited specific energy. In this regard, the voltage window of the Na5VP||Al/C cell was initially tested between 1.0 and 3.8 V versus Na/Na$^+$, proceeding with the three-electron redox reaction (between Na1VP and Na4VP). To further verify the structural reversibility during charge/discharge, the detailed phase transition from

Na1VP to Na4VP and corresponding volumes of the Na1VP, Na3VP, and Na4VP supercells were determined by the Rietveld refinement of the operando XRD, as shown in Figure S13. The lattice parameter c representing the interlayer distance of Na3VP decreases, whereas the lattice parameter a corresponding to the basal dimension increases upon sodiation to 1.0 V (Figure S13B). The reduced c parameter can be attributed to the decreased electrostatic repulsion between O^{2-} layers as the Na$^+$ layer is continuously filled, while the increased a parameter is associated with the expansion of vanadium octahedra because of the electrochemical reduction of vanadium ions.[54] The volume expansion from pristine Na3VP to Na4VP is ~3.0%, while a volume shrinkage of 9.2% takes place upon the transition from pristine Na3VP to Na1VP, consistent with the DFT result. The small volume change during Na insertion and extraction can explain the excellent cyclic performance (see the discussion below). Moreover, the second charge/ discharge cycle shows the same profile as that of the first cycle, which reflects the excellent reversibility of the Na3VP within 1.0–3.8 V. The cyclic performance of Na5VP||Al/C cell was then examined at 2C. As shown in Figure 4B, the initial discharge capacity was approximately 145 mAh g_{Na5VP}^{-1} with a retained specific capacity of 135 mAh g_{Na5VP}^{-1} after 130 cycles, corresponding to a high capacity retention of ≈93%. In contrast, the corresponding specific capacity of the Na3VP||Al/C cell was only 68.9 mAh g_{Na3VP}^{-1} with more than 30% capacity fade after 130 cycles. In addition, the GCD curves of Na5VP||Al/C cell were

nearly unchanged after 130 cycles, which is critical for retaining high energy efficiency (Figure 4C).

It is of interest to compare the rate performance of the Na5VP||Al/C and Na3VP||Al/C cells. As displayed in Figure 4D, the specific discharge capacities of the Na5VP||Al/C cell were 150.0, 147.5, 143.2, and 131.3 mAh g_{Na5VP}^{-1} at current densities of 0.5C, 1C, 2C, and 5C, respectively. In contrast, the Na3VP||Al/C cell generally delivered lower discharge capacities at various current densities (e.g., 89.6 and 72.7 mAh g_{Na3VP}^{-1} at 2C and 5C, respectively). In addition, the Na3VP||Al/C cell exhibited a fast capacity decay from 81.9 to 64.5 mAh g_{Na3VP}^{-1} at 5C within 10 cycles, primarily because of the continuous and rapid depletion of the Na source in the Na3VP cathode. Impressively, the Na5VP||Al/C cell exhibited much better cyclability owing to the existence of a Na reservoir on the anode side. High energy efficiencies are of significant interest for the practical applications of a battery system.[55] The energy efficiencies of the Na5VP||Al/C cell were calculated to be 92.3%, 91.0%, and 87.8% at 0.5C, 1C, and 2C, respectively (Figure S14). Notably, the energy efficiency for the current Na5VP||Al/C cell is comparable to those of the commercialized LIBs.[56] Such superior energy storage efficiency is attributed to the ultrafast Na insertion/extraction kinetics in the NASICON-structured cathode and rapid Na plating/stripping dynamics at the anode.

To achieve a longer lifespan, we also narrowed the voltage window of the Na5VP||Al/C cell within 3.0–3.8 V versus Na/Na$^+$, as shown in Figure 5A. After activation at 0.5C for three cycles, the Na5VP||Al/C cell delivered a high initial capacity of 97 mAh g_{Na5VP}^{-1} and negligible capacity fade (0.017% per cycle) for 300 cycles at 2C (Figure 5B). The GCD curves reveal that the working voltage of the Na5VP||Al/C battery almost did not decrease (Figure S15). The energy efficiency was maintained above 95.4% at the 300th cycle, confirming the outstanding
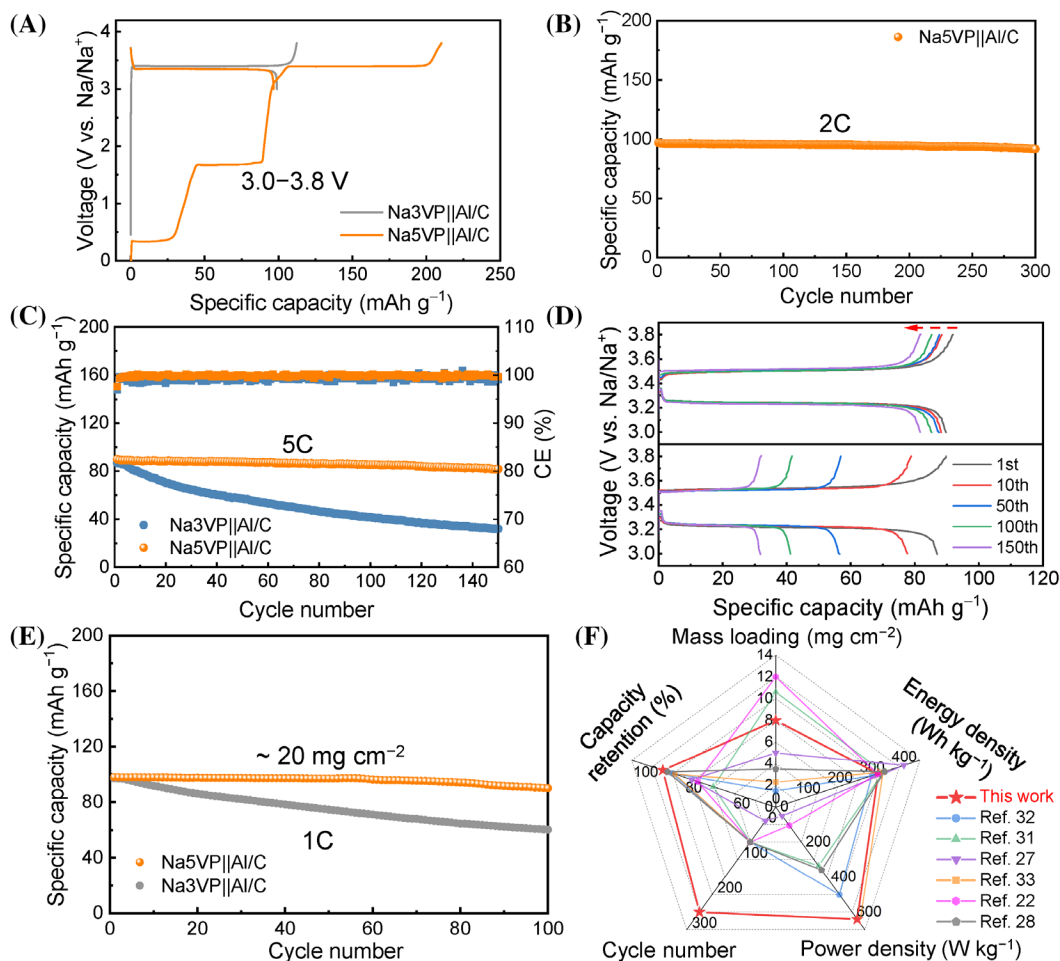

FIGURE 5 Electrochemical performance of the Na5VP||Al/C cells within the voltage window of 3.0–3.8 V versus Na/Na$^+$. (A) Initial GCD profiles of Na5VP||Al/C and Na3VP||Al/C cells at 0.5C. (B) Cyclic performance of the Na5VP||Al/C cell at 2C. (C) Cyclic performance and (D) the corresponding GCD profiles at a high current density of 5C. (E) Cyclic performance of Na5VP||Al/C cell with thick electrodes at 1C. (F) Radar plot of Na5VP||Al/C cell (data from Figure 5B) compared with previously reported SFA-SMBs.[22,27,28,31–33] GCD, galvanostatic charge–discharge; SFA, sodium-free-anode; SMBs, sodium metal batteries

stability of the Na5VP||Al/C battery. The morphologies of Na5VP and Al/C electrodes cycled after 300 cycles at 2C were analyzed by SEM, as shown in Figure S16A–D. The cycled cathode maintained a spherical morphology without obvious cracks. The Na deposition on Al/C current collector was homogenous and smooth without dendrites. In addition, the high-resolution TEM image suggests that the pristine Na5VP was transformed to Na3VP within the voltage range of 3.0–3.8 V (Figure S16E), as illustrated in Figure 1B. Even after cycling at a high current density of 5C, the Na5VP||Al/C cell retained a capacity of 86 mAh g_{Na5VP}^{-1} after 150 cycles with a capacity retention of 95% (Figure 5C,D). On the contrary, the Na3VP||Al/C cell displayed much worse cyclic stability with a much lower capacity of 31.9 mAh g_{Na3VP}^{-1} after 150 cycles. The rate performance of the Na5VP||Al/C cell revealed that the Na5VP||Al/C cells show much better stability compared to Na3VP||Al/C, particularly at a high current of 5C (Figure S17).

In addition, the SMF-SMB performance obtained using the Na5VP electrode with direct contact with Na metal was also assessed at 1C. As shown in Figure S18, when the sodiation time was 5 min, the resultant Na5VP||Al/C cell displayed similar cyclic stability at 1C to that of the battery using the galvanostatically presodiated Na5VP. The sodium ion diffusion coefficient value (D_{Na}^{+}) was estimated by measuring the electrochemical impedance spectroscopy (EIS). Figure S19 shows the Nyquist plots of the Na5VP||Al/C and Na5VP||Al cells, which consist of a depressed semicircle in the high-frequency region and a quasi-straight line in the low-frequency region. Moreover, the D_{Na}^{+} values for the Na5VP and Na3VP electrodes were calculated to be 7.145×10^{-15} and 2.818×10^{-14} cm² s^{-1}, respectively (see Supporting Information). Although the D_{Na}^{+} of Na5VP was slightly lower than that of Na3VP, the

reaction paths were the same after the extraction of two Na atoms in the lattice during the first charge process.

To demonstrate their feasibility in real-world applications, we evaluated the cyclic performances of the Na5VP||Al/C and Na3VP||Al/C cells with a high cathode mass loading of ~20 mg cm^{-2}. As shown in Figure 5E, the Na5VP||Al/C displayed capacity retention of 92% after 100 cycles, while that of the Na3VP||Al/C was only 62%. The comparison of the electrochemical performance of the Na5VP||Al/C cell to those of other SFA-SMBs reveals that the Na5VP||Al/C cell delivers a relatively high power density (640 W kg^{-1}) associated with a high energy density of 320 Wh kg^{-1} even after 300 cycles (Figure 5F).[22,27,28,31–33] The presodiated FeS$_2$||Al/C cell exhibits a slightly higher specific energy but with a low power density, short lifespan, and poor capacity retention because of the structural degradation of presodiated FeS$_2$. The Na$_2$Fe$_2$(CN)$_6$||Cu cell with comparable specific energy displays much inferior specific power and cycle life. Overall, the Na5VP||Al/C cell in this work outperformed all counterparts in terms of cyclability and power densities.

Further comparison of Na5VP||Al/C cells with recently reported Na-based full-cell configurations in terms of sodium storage capacity (including all the active electrode materials), average output voltage, and specific energy/power was carried out.[27,31,32,57–61] As shown in Figure 6A, the as-designed Na5VP||Al/C SFA-SMB offers an average voltage and capacity of ~2.7 V and ~150 mAh g_{Na5VP}^{-1} within the voltage range of 1.0–3.8 V versus Na/Na$^+$. In contrast, the Na$_{0.7}$CoO$_2$||graphite batteries present both a lower capacity and average voltage, resulting in a specific energy density lower than 100 Wh kg^{-1}. Although the Na$_{1.5}$VPO$_{4.8}$F$_{0.7}$||graphite,[62] P2-Na$_{0.67}$Ni$_{0.23}$Mg$_{0.1}$Mn$_{0.67}$O$_2$||hard carbon,[60] and NaVPO$_4$F||Na-Sb@ZMF/C[57] cells exhibited high output voltages, the specific capacity and energy density were far
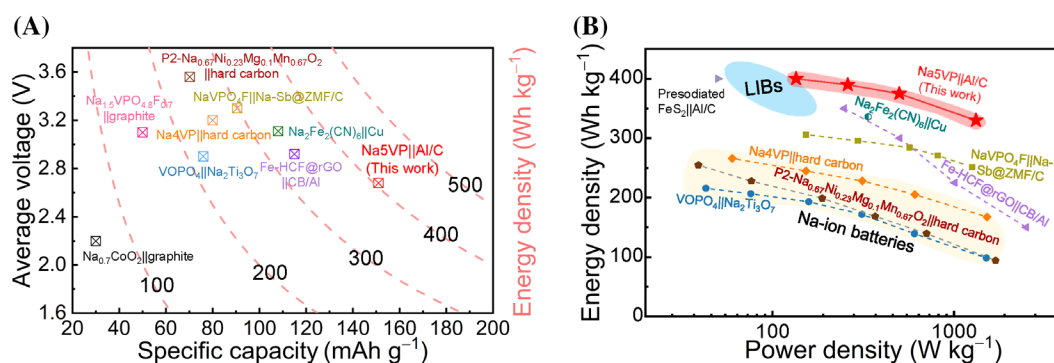

FIGURE 6 (A) Comparison of the average voltage and capacity of Na5VP||Al/C cell with other recently reported Na-ion and Na-metal batteries.[31,32,57–60,62] (B) Ragone plots the Na5VP||Al/C cell as compared with the previously reported SFA-SMBs, Na-ion batteries, and the current LIBs.[27,31,32,57–60] The total active mass of both electrodes (cathode and anode) was included for calculating the power and energy densities. LIBs, lithium-ion batteries; SFA, sodium-free-anode; SMBs, sodium metal batteries

from satisfactory. The Ragone plots in Figure 6B show that the Na5VP||Al/C cells exhibited an ultrahigh specific energy density of ~400 Wh kg^{-1} (including all the active electrode materials) at a specific power of ~133 W kg^{-1} (see Supporting Information). When the specific power density was 1320 W kg^{-1}, the Na5VP||Al/C cell maintained a specific energy density of 330 Wh kg^{-1}. The above results demonstrate that the electrochemical performance of the present Na5VP||Al/C cell is superior to those of other SFA-SMBs,[27,31,32] Na-metal batteries,[57] and Na-ion batteries,[58–60] and is comparable with state-of-the-art LIBs.[63,64] We further fabricated pouch cells to demonstrate the practical feasibility of Na5VP||Al/C cell (Figure Figure S20A). The pouch cell can steadily power a 1.2-meter-long LED strip even under folding and cutting (Figure S20B,C), proving its outstanding flexibility and safety.

In summary, the conventional Na3VP||Al/C cells can only realize the insertion and extraction of two Na ions per formula of Na3VP (Na3VP → Na1VP) without additional Na replenishers, thus resulting in a low specific capacity and fast capacity decay, especially at high rates. The reversible sodiation in the Na3VP cathode significantly improved the overall electrochemical performance of the Na3VP||Al/C cell in terms of sodium storage capacity, kinetics, and stability. For operation in the wide voltage window of 1.0–3.8 V versus Na/Na^{+}, the phase transition occurring at the low-voltage plateau of 1.7 V (Na4VP → Na3VP) further increased the specific energy density of the SFA-SMB. In addition to the significantly improved electrochemical performance, the developed presodiation approach has two merits: (i) the prestored Na in Na5VP can be completely converted to active Na without the introduction of inactive elements and (ii) the supplementary Na prestored in the Na5VP lattice is more stable than the metallic Na, which largely diminishes the safety concerns for battery fabrication, storage, and transportation (Figure S21). The abundant natural resources of Na coupling with the decreased cost of processing anodes without Na metal enable the Na5VP||Al/C SFA-SMBs as a more sustainable and economically viable option for energy storage applications.

3 | CONCLUSIONS

For the first time, sodium-rich NASICON-structured cathodes were developed for the simple construction of high-performance SFA-SMBs. In the fabricated Na5VP||Al/C cell, the prestored Na in Na5VP serves as a replenisher to effectively offset the Na loss during long-term Na plating/stripping cycles. Furthermore, the excellent structural and electrochemical reversibility of Na5VP was comprehensively revealed by operando XRD, electrochemical tests, and DFT

calculations. The highly reversible phase transition from Na4VP to Na1VP in the voltage window of 1.0–3.8 V versus Na/Na^{+} resulted in an ultrahigh energy density of ~400 Wh kg^{-1} and good cyclic stability in SFA-SMBs. For operation in the narrow voltage window of 3.0–3.8 V, the lifespan was further extended over 300 cycles, accompanied by a high energy density of 320 Wh kg^{-1} and power density of 640 W kg^{-1}. These results verify that the reversible presodiation strategy is highly efficient and feasible to increase the energy density and lifespan of SFA-SMBs, which can be extended to other metal-free anode battery systems.

4 | EXPERIMENTAL SECTION

4.1 | Preparation of Na3VP electrode

Na3VP (Hubei Energy Technology Co., Ltd.), acetylene black (Alfa Aesar Co., Ltd.), and polyvinylidene fluoride (PVDF, MTI Co., Ltd.) were first homogenized in N-methyl pyrrolidinone (NMP, Sigma Aldrich) at a mass ratio of 90:5:5. Then, the slurry was spread on a carbon-coated Al foil (MTI Co., Ltd., coating thickness: 1 μm) by a doctor blade and dried at 80°C for 12 h in a vacuum oven. The electrodes were punched into discs (12 mm in diameter) with a typical Na3VP mass loading of ~7 mg cm^{-2}.

4.2 | Preparation of Na5VP electrode

Typically, the presodiated cathodes were fabricated by electrochemical methods. Na3VP half-cells were assembled in CR2025-type coin cells using a Na3VP cathode as the working electrode, a Na foil as the counter electrode, a Celgard 2500 membrane as the separator, and a diglyme solution containing 1.0 M sodium hexafluorophosphate (NaPF$_6$) as the electrolyte. To fabricate Na5VP cathodes, these Na3VP half-cells were first discharged from the open circuit potential to 0.1 V versus Na/Na^{+} at 0.2C. After that, the Na5VP cathodes were obtained by disassembling the coin cells. In addition to the assembly of half-cells, we also carried out a facile presodiation strategy by directly stacking the metallic Na foil to the Na3VP electrodes with a tiny amount of electrolyte (20 μl) for 5 min to obtain Na5VP cathodes. Regarding the highly sensitive Na metal, all the experiments were conducted in an Ar-filled glove box.

4.3 | Characterizations

The XRD patterns were collected using a Rigaku SmartLab diffractometer with Cu Kα radiation ($\lambda = 1.5405$ Å) in a

scan range (2θ) of 10–80°. SEM images of Na3VP and Na5VP electrodes were obtained with a Tescan VEGA3 microscope, while the TEM/HRTEM images were taken using a JEOL 2100F STEM/EDS microscope. XPS was measured by a Thermo Scientific Nexsa with Al Kα radiation as the excitation source. Operando XRD was employed to study the phase transition of Na3VP during charging/discharging processes. The data for every single pattern were collected for 10 min with a scan range (2θ) between 18° and 38°. The morphology of Na plating on Al/C and Al was examined by SEM (Hitachi S-8100), operated at 5.0 kV. Specifically, the disassembled samples were washed with 1,2-dimethoxyethane and transferred to the SEM chamber using an Ar-filled container.

4.4 | Electrochemical measurements

To evaluate Na plating/stripping efficiencies, CR2025-type coin cells were assembled inside the glove box using Al/C or Al as the working electrode ($\phi16$ mm), Na foil ($\phi14$ mm) as the counter/reference electrodes with a Celgard 2400 separator, and 50 µl electrolyte. The cells were cycled between 0 and 0.5 V versus Na/Na$^+$ at 50 µA cm^{-2} for the first five cycles to reduce the surface contamination. Then 1.0 mAh cm^{-2} of Na was deposited on the collectors at different areal currents and recharged to 0.5 V to strip the predeposited Na. The CE is defined as the ratio of stripped capacity to plated capacity. SFA-SMBs were assembled using a presodiated Na5VP or Na3VP cathode, an Al/C foil (anode current collector), a double-layered separator consisting of a Whatman glass fiber and a Celgard 2500 film, and ~60 µl of electrolyte (1.0 M NaPF$_6$ in diglyme). To fabricate the pouch cell, the Na5VP cathode film with 43 mm width and 56 mm length was first prepared by the direct-contact method. Afterward, the glass fiber, Celgard 2500 film, and Al/C current collector were piled up in sequence. Finally, ~800 µl of the 1.0 M NaPF$_6$ in diglyme electrolyte was injected into the cell and the pouch cell was sealed. GCD tests were conducted within voltage windows of 1.0–3.8 or 3.0–3.8 V using battery testers (Wuhan Land CT2001A, China) at 25°C at various C rates. CV measurement was performed using an electrochemical workstation (Autolab PGSTAT302N, Netherlands) between 0.1 and 3.8 V at a scan rate of 0.2 mV s^{-1}. EIS was conducted in the range of frequency from 10 mHz to 100 kHz on the same workstation.

4.5 | Computational methods

All spin-polarized DFT calculations were performed under the general gradient approximation (GGA) using the Perdew–Burke–Ernzerhof (PBE) functionals as implemented in the Vienna ab initio simulation package (VASP).[65,66] The core-electrons were treated with the projector augmented wave method. A high U value of 4.2 eV was used for the vanadium atom to reflect the strong Coulomb corrections.[67] An energy cutoff of 520 eV was used with a $3 \times 3 \times 2$ Monkhorst k-points sampling. For each structural relaxation, both the ion positions and the lattice parameters were allowed to change until the Hellman–Feynman forces on each ion dropped below 0.02 eV Å^{-1}, and the convergence condition for energy was 10^{-5} eV.

CONFLICT OF INTEREST
The authors declare no conflict of interest.

ORCID
Junxiong Wu https://orcid.org/0000-0002-4798-8197
Cong Lin https://orcid.org/0000-0003-0021-5055
Jiapeng Liu https://orcid.org/0000-0001-8667-1929
Xiaoliang Yu https://orcid.org/0000-0003-3431-3868

REFERENCES
1. Armand M, Tarascon JM. Building better batteries. *Nature*. 2008;451(7179):652-657.
2. Li M, Lu J, Ji X, et al. Design strategies for nonaqueous multivalent-ion and monovalent-ion battery anodes. *Nat Rev Mater*. 2020;5(4):276-294.
3. Fan LZ, He H, Nan CW. Tailoring inorganic–polymer composites for the mass production of solid-state batteries. *Nat Rev Mater*. 2021;(6):1003-1019.
4. Ma L, Lv Y, Wu J, et al. Recent advances in anode materials for potassium-ion batteries: a review. *Nano Res*. 2021;(14):4442-4470.
5. Wu J, Liang Q, Yu X, et al. Deep eutectic solvents for boosting electrochemical energy storage and conversion: a review and perspective. *Adv Funct Mater*. 2021;31(22):2011102.

6. Zhang L, Qin X, Zhao S, et al. Advanced matrixes for binder-free nanostructured electrodes in lithium-ion batteries. *Adv Mater*. 2020;32(24):1908445.

7. Jaumaux P, Wu J, Shanmukaraj D, et al. Non-flammable liquid and quasi-solid electrolytes toward highly-safe alkali metal-based batteries. *Adv Funct Mater*. 2021;31(10):2008644.

8. Tarascon JM. Na-ion versus Li-ion batteries: complementarity rather than competitiveness. *Joule*. 2020;4(8):1616-1620.

9. Wang H, Matios E, Luo J, Li W. Combining theories and experiments to understand the sodium nucleation behavior towards safe sodium metal batteries. *Chem Soc Rev*. 2020;49(12):3783-3805.

10. Wu J, Ihsan-Ul-Haq M, Ciucci F, Huang B, Kim J-K. Rationally designed nanostructured metal chalcogenides for advanced sodium-ion batteries. *Energy Storage Mater*. 2021;34:582-628.

11. Xu X, Zhou D, Qin X, et al. A room-temperature sodium–sulfur battery with high capacity and stable cycling performance. *Nat Commun*. 2018;9(1):3870.

12. Wang Q, Ge X, Xu J, et al. Fabrication of microporous sulfur-doped carbon microtubes for high-performance sodium-ion batteries. *ACS Appl Energy Mater*. 2018;1(11):6638-6645.

13. Zhang Z, Du Y, Wang Q-C, et al. A yolk–Shell-structured $FePO_4$ cathode for high-rate and long-cycling sodium-ion batteries. *Angew Chem Int Ed*. 2020;59(40):17504-17510.

14. Pan W, Guan W, Jiang Y. Research advances in polyanion-type cathodes for sodium-ion batteries. *Acta Phys Chim Sin*. 2020;36(5):1905017.

15. Wu J, Zou P, Ihsan-Ul-Haq M, et al. Sodiophilically graded gold coating on carbon skeletons for highly stable sodium metal anodes. *Small*. 2020;16(40):2003815.

16. Sun B, Li P, Zhang J, et al. Dendrite-free sodium-metal anodes for high-energy sodium-metal batteries. *Adv Mater*. 2018;30(29):1801334.

17. Seh ZW, Sun J, Sun Y, Cui Y. A highly reversible room-temperature sodium metal anode. *ACS Cent Sci*. 2015;1(8):449-455.

18. Hu X, Matios E, Zhang Y, et al. Deeply cycled sodium metal anodes at low temperature and in lean electrolyte conditions. *Angew Chem Int Ed*. 2021;60(11):5978-5983.

19. Liu W, Chen Z, Zhang Z, et al. Lithium-activated SnS–graphene alternating nanolayers enable dendrite-free cycling of thin sodium metal anodes in carbonate electrolyte. *Energy Environ Sci*. 2021;14(1):382-395.

20. Jin X, Zhao Y, Shen Z, et al. Interfacial design principle of sodiophilicity-regulated interlayer deposition in a sandwiched sodium metal anode. *Energy Storage Mater*. 2020;31:221-229.

21. Mubarak N, Rehman F, Wu J, et al. Morphology, chemistry, performance trident: insights from hollow, mesoporous carbon nanofibers for dendrite-free sodium metal batteries. *Nano Energy*. 2021;86:106132.

22. Cohn AP, Metke T, Donohue J, et al. Rethinking sodium-ion anodes as nucleation layers for anode-free batteries. *J Mater Chem A*. 2018;6(46):23875-23884.

23. Ma L, Wu J, Zhu G, et al. Recent advances in two-dimensional materials for alkali metal anodes. *J Mater Chem A*. 2021;9(9):5232-5257.

24. Yu X, Xue L, Goodenough JB, Manthiram A. A high-performance all-solid-state sodium battery with a poly(ethylene oxide)–$Na_3Zr_2Si_2PO_{12}$ composite electrolyte. *ACS Mater Lett*. 2019;1(1):132-138.

25. Lyu YQ, Yu J, Wu J, Effat MB, Ciucci F. Stabilizing Na-metal batteries with a manganese oxide cathode using a solid-state composite electrolyte. *J Power Sources*. 2019;416:21-28.

26. Wang A, Hu X, Tang H, et al. Processable and moldable sodium-metal anodes. *Angew Chem Int Ed*. 2017;56(39):11921-11926.

27. Cohn AP, Muralidharan N, Carter R, Share K, Pint CL. Anode-free sodium battery through in situ plating of sodium metal. *Nano Lett*. 2017;17(2):1296-1301.

28. Lee ME, Lee S, Choi J, et al. Anode-free sodium metal batteries based on nanohybrid core–shell templates. *Small*. 2019;15(37):1901274.

29. Nanda S, Gupta A, Manthiram A. Anode-free full cells: a pathway to high-energy density lithium-metal batteries. *Adv Energy Mater*. 2021;11(2):2000804.

30. Wang H, Wu Y, Liu S, et al. 3D ag@C cloth for stable anode free sodium metal batteries. *Small Methods*. 2021;5(4):2001050.

31. Rudola A, Gajjela SR, Balaya P. High energy density in-situ sodium plated battery with current collector foil as anode. *Electrochem Commun*. 2018;86:157-160.

32. Mazzali F, Orzech MW, Adomkevicius A, et al. Designing a high-power sodium-ion battery by in situ metal plating. *ACS Appl Energy Mater*. 2019;2(1):344-353.

33. Ma B, Lee Y, Bai P. Dynamic interfacial stability confirmed by microscopic optical operando experiments enables high-retention-rate anode-free Na metal full cells. *Adv Sci*. 2021;8(12):2005006.

34. Lin L, Qin K, Zhang Q, et al. Li-rich $Li_2[Ni_{0.8}Co_{0.1}Mn_{0.1}]O_2$ for anode-free lithium metal batteries. *Angew Chem Int Ed*. 2021;60(15):8289-8296.

35. Qiao Y, Yang H, Chang Z, et al. A high-energy-density and long-life initial-anode-free lithium battery enabled by a Li_2O sacrificial agent. *Nat Energy*. 2021;6(6):653-662.

36. Shanmukaraj D, Kretschmer K, Sahu T, et al. Highly efficient, cost effective, and safe sodiation agent for high-performance sodium-ion batteries. *ChemSusChem*. 2018;11(18):3286-3291.

37. Niu YB, Guo YJ, Yin YX, et al. High-efficiency cathode sodium compensation for sodium-ion batteries. *Adv Mater*. 2020;32(33):2001419.

38. Liu X, Tan Y, Wang W, et al. Ultrafine sodium sulfide clusters confined in carbon nano-polyhedrons as high-efficiency presodiation reagents for sodium-ion batteries. *ACS Appl Mater Interfaces*. 2021;13(23):27057-27065.

39. Zhang B, Dugas R, Rousse G, et al. Insertion compounds and composites made by ball milling for advanced sodium-ion batteries. *Nat Commun*. 2016;7(1):10308.

40. Martinez DIJ, Otaegui L, López del Amo JM, Armand M, Singh G. NaN_3 addition, a strategy to overcome the problem of sodium deficiency in P2-$Na_{0.67}[Fe_{0.5}Mn_{0.5}]O_2$ cathode for sodium-ion battery. *J Power Sources*. 2017;337:197-203.

41. Moeez I, Jung HG, Lim HD, Chung KY. Presodiation strategies and their effect on electrode–electrolyte interphases for high-performance electrodes for sodium-ion batteries. *ACS Appl Mater Interfaces*. 2019;11(44):41394-41401.

42. Liu X, Tan Y, Liu T, et al. A simple electrode-level chemical presodiation route by solution spraying to improve the energy density of sodium-ion batteries. *Adv Funct Mater*. 2019;29(50):1903795.

43. Zou K, Deng W, Cai P, et al. Prelithiation/presodiation techniques for advanced electrochemical energy storage systems:

concepts, applications, and perspectives. *Adv Funct Mater.* 2021;31(5):2005581.

44. Jian Z, Hu YS, Ji X, Chen W. NASICON-structured materials for energy storage. *Adv Mater.* 2017;29(20):1601925.

45. Gu E, Liu S, Zhang Z, et al. An efficient sodium-ion battery consisting of reduced graphene oxide bonded $Na_3V_2(PO_4)_3$ in a composite carbon network. *J Alloys Compd.* 2018;767:131-140.

46. Jian Z, Sun Y, Ji X. A new low-voltage plateau of $Na_3V_2(PO_4)_3$ as an anode for Na-ion batteries. *Chem Commun.* 2015;51(29):6381-6383.

47. Liang L, Li X, Zhao F, et al. Construction and operating mechanism of high-rate Mo-doped $Na_3V_2(PO_4)_3$@C nanowires toward practicable wide-temperature-tolerance Na-ion and hybrid Li-/Na-ion batteries. *Adv Energy Mater.* 2021;11(21):2100287.

48. Sun S, Chen Y, Cheng J, et al. Constructing dimensional gradient structure of $Na_3V_2(PO_4)_3$/C@CNTs-WC by wolfram substitution for superior sodium storage. *Chem Eng J.* 2021;420:130453.

49. Jian Z, Han W, Lu X, et al. Superior electrochemical performance and storage mechanism of $Na_3V_2(PO_4)_3$ cathode for room-temperature sodium-ion batteries. *Adv Energy Mater.* 2013;3(2):156-160.

50. Wang C, Wang S, He YB, et al. Combining fast Li-ion battery cycling with large volumetric energy density: grain boundary induced high electronic and ionic conductivity in $Li_4Ti_5O_{12}$ spheres of densely packed nanocrystallites. *Chem Mater.* 2015;27(16):5647-5656.

51. Xu J, Gu E, Zhang Z, et al. Fabrication of porous $Na_3V_2(PO_4)_3$/reduced graphene oxide hollow spheres with enhanced sodium storage performance. *J Colloid Interface Sci.* 2020;567:84-91.

52. Gu E, Xu J, Du Y, et al. Understanding the influence of different carbon matrix on the electrochemical performance of $Na_3V_2(PO_4)_3$ cathode for sodium-ion batteries. *J Alloys Compd.* 2019;788:240-247.

53. Yao X, Zhu Z, Li Q, et al. 3.0 V high energy density symmetric sodium-ion battery: $Na_4V_2(PO_4)_3\|Na_3V_2(PO_4)_3$. *ACS Appl Mater Interfaces.* 2018;10(12):10022-10028.

54. Xu Z-L, Park J, Wang J, et al. A new high-voltage calcium intercalation host for ultra-stable and high-power calcium rechargeable batteries. *Nat Commun.* 2021;12(1):3369.

55. Eftekhari A. Energy efficiency: a critically important but neglected factor in battery research. *Sustain Energy Fuels.* 2017;1(10):2053-2060.

56. Farhad S, Nazari A. Introducing the energy efficiency map of lithium-ion batteries. *Int J Energy Res.* 2019;43(2):931-944.

57. Liu S, Bai M, Tang X, et al. Enabling high-performance sodium metal anode via a presodiated alloy-induced interphase. *Chem Eng J.* 2021;417:128997.

58. Li H, Peng L, Zhu Y, et al. An advanced high-energy sodium ion full battery based on nanostructured $Na_2Ti_3O_7$/$VOPO_4$ layered materials. *Energy Environ Sci.* 2016;9(11):3399-3405.

59. Mirza S, Song Z, Zhang H, et al. A simple pre-sodiation strategy to improve the performance and energy density of sodium ion batteries with $Na_4V_2(PO_4)_3$ as the cathode material. *J Mater Chem A.* 2020;8(44):23368-23375.

60. Peng B, Sun Z, Zhao L, Li J, Zhang G. Dual-manipulation on P2-$Na_{0.67}Ni_{0.33}Mn_{0.67}O_2$ layered cathode toward sodium-ion full cell with record operating voltage beyond 3.5 V. *Energy Storage Mater.* 2021;35:620-629.

61. Hasa I, Dou X, Buchholz D, et al. A sodium-ion battery exploiting layered oxide cathode, graphite anode and glyme-based electrolyte. *J Power Sources.* 2016;310:26-31.

62. Xu Z-L, Yoon G, Park KY, et al. Tailoring sodium intercalation in graphite for high energy and power sodium ion batteries. *Nat Commun.* 2019;10(1):2598.

63. Shen Y, Qian J, Yang H, Zhong F, Ai X. Chemically prelithiated hard-carbon anode for high power and high capacity Li-ion batteries. *Small.* 2020;16(7):1907602.

64. Shen Y, Shen X, Yang M, et al. Achieving desirable initial coulombic efficiencies and full capacity utilization of Li-ion batteries by chemical prelithiation of graphite anode. *Adv Funct Mater.* 2021;31(24):2101181.

65. Kresse G, Furthmüller J. Efficient iterative schemes for ab initio total-energy calculations using a plane-wave basis set. *Phys Rev B.* 1996;54(16):11169-11186.

66. Perdew JP, Burke K, Ernzerhof M. Generalized gradient approximation made simple. *Phys Rev Lett.* 1996;77(18):3865-3868.

67. Wang L, Maxisch T, Ceder G. Oxidation energies of transition metal oxides within the GGA + U framework. *Phys Rev B.* 2006;73(19):195107.

SUPPORTING INFORMATION

Additional supporting information may be found in the online version of the article at the publisher's website.